CFD Analysis of Mechanisms Underlying the Porosity-reducing Effect of Atomized Flows in High-pressure Die Cast Products

Eitaro Koya[1,*] *Masahiko* Nakagawa[1], *Shinya* Kitagawa[1], *Jun* Ishimoto[2], *Yoshikatsu* Nakano[2] *and Nao*ya Ochiai[2]

[1]Honda Motor Co., Ltd, Motorcycle Operations, 3-15-1, Senzui, Asaka, Japan
[2]Tohoku University, Institute of Fluid Science, 2-1-1, Katahira, Sendai, Japan

Abstract. In high-pressure die casting, attention has been paid to the J factor, which is defined by the speed of the metal injected at the gate and the shape of the gate. In casting experiments using a piston die, the porosity of the product can be reduced by increasing the J factor such that the metal flow passing through the gate forms an atomized flow. To clarify the underlying mechanisms, we developed a system for simulating a two-phase flow of air and aluminum by large-scale calculations of turbulent flow. During the development of the system, we injected metal into an open space and performed imaging to confirm the state of the atomized flow. The system was then verified by reproducing the atomized flow. The analysis results visualized the many small turbulent vortices generated in the thick part far from the gate. We demonstrated that the change from small to longitudinal vortices promoted entrainment of air into the aluminum and increased the efficiency of air expulsion outside the die through an increase in the J factor.

1 Introduction

High-pressure die casting (HPDC) is a method of casting at high speed and high pressure that offers the advantages of rapid cooling and production of fine microstructures. For example, the use of HPDC to fabricate pistons takes advantage of these characteristics. In this example, an Al-Si alloy with a Si content above the eutectic composition was used to form a fine network of eutectic silicon and intermetallic compounds surrounding α-phase aluminum, thereby improving high-temperature strength [1]. However, one issue with HPDC is that the strength of manufactured pieces is degraded by porosity arising from gases such as air that are entrained into the metal when it is injected into the die at high speed. Approaches for solving this issue have generally involved use of a strong vacuum or substitution of oxygen in the cavity [1,2]. In addition, a localized high-pressure squeezing method is applied to the thicker areas of manufactured parts to reduce porosity.

Another approach to reducing porosity focuses on the J factor, which is defined by the speed of the metal injected at the gate and the shape of the gate. If the J factor exceeds some threshold value, the metal flow atomizes when it passes through the gate. It has been reported that when the J factor is further increased (the high J factor method), the mechanical properties of HPDC products are enhanced and porosity is reduced [3, 4]. If the quality of HPDC can be enhanced by increasing the J factor, then it would be possible to manufacture high-quality HPDC parts inexpensively by using a general-purpose casting machine without the need for specialized equipment with features such as complex injection mechanisms, dies with complicated seal mechanisms, and auxiliary pressure application devices.

However, the mechanisms underlying the reduction in porosity through the use of a high J factor are not yet clear, and attempts are being made to clarify them [5]. To accomplish this, it is necessary to visualize the flow within the die during HPDC. Attempts to do so have been made using photographic methods but have so far been unsuccessful in capturing high-speed molten flow at microscopic resolutions [6].

In computational fluid dynamics (CFD), large-scale turbulence simulations using high-speed computational processing (e.g., parallel processing) are being applied to understand an increasingly wide variety of phenomena. Against this background, research has been conducted into basic simulations to reproduce the injection condition of the metal at the gate in order to visualize the flow during HPDC [7].

In this study, we modeled an actual casting die design and developed a simulation system to reproduce the experimental results of a casting experiment involving a piston die. The aim of the developed system was to visualize and quantify the detailed state of the air inside the die by using two-phase flow calculations of the air within the molten aluminum.

This paper first presents the results photographic experiments examining various J factors used for the metal interface at the gate and discusses the actual state of the atomized flow. Next, the aluminum filling and air expulsion processes within the cavity of the piston die are investigated using CFD. Finally, the results are

* Corresponding author: eitaro_koya@jp.honda

explained by discussing the mechanisms underlying the reduction in porosity with a higher J factor.

2 Casting experiment on J factor and porosity

2.1. Casting experiment methods

To investigate the relationship between the J factor and the internal quality of HPDC parts, we performed a casting experiment using a piston-shaped die that examined the relationship between the J factor and the porosity of the thicker parts of the piston. The flow state when the metal passes through the gate in HPDC is defined by the J factor in the following equationaccording to Wallace [8]:

$$\mathrm{J} = D \times \rho \times V_g^{1.71} \quad (1)$$

Here, V_g is the ingate speed of the metal, ρ is the specific gravity of the metal, and D is the gate shape factor defined by gate area A_g, gate depth a, and gate width b as follows:

$$D = A_g/(a + (a + b) \times 2) \quad (2)$$

As the J factor becomes larger, the flow of metal at the gate changes from a continuous jet to a coarse particle flow and then to an atomized flow. In the case of aluminum, the threshold J factor for atomization is 1064. Figure 1 shows the shape of the cast piston and the gate shape. In the casting experiment, a two-piece die was used, and the J factor was changed by changing the highinjection speed with a constant low injection speed. The die uses chill vents that are open to the atmosphere; no vacuum equipment was used. The piston diameter was 54 mm and its weight was 90 g. A casting machine with a die cramping force of 350 tons was used for casting. The casting pressure was 70 MPa. The material used was an Al-13%Si-3.5%Cu-1.5%Mg alloy.

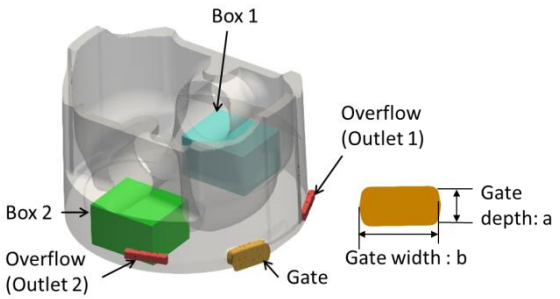

Fig. 1. Test piston shape and gate shape

2.2 Relationship between J factor and porosity

The amount of porosity in the areas labeled Box 1 and Box 2 in Figure 1 was measured with a 225-kV flat-panel micro computed tomography (micro-CT) scanner. Imaging was performed at a resolution of 20 μm, and the porosity was derived by imaging processing. Figure 2 shows the derived porosity images. The porosity measurement points in the thick parts (i.e., the pin boss areas) of the piston are taken as Box 1 and Box 2, and the relationship between the porosity volume fraction and J factor at each of these locations is shown in Figure 3. When the J factor was increased from 1000 to 2000, the porosity volume fraction was greatly reduced. Above 2000, a trend was observed in which the rate of reduction decreased and saturated. This clarified the trend of porosity decreasing as the J factor increased. Furthermore, at the low J factor of 1000, the porosity volume fraction in Box 1 was 1.5 times that in Box 2.

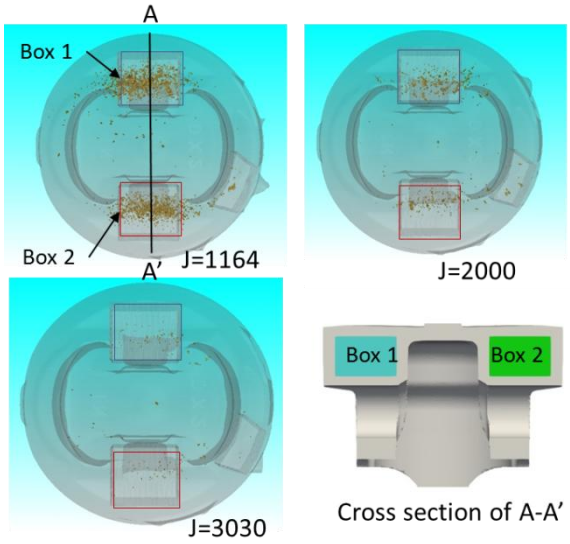

Fig. 2. Porosity images derived from micro-CT

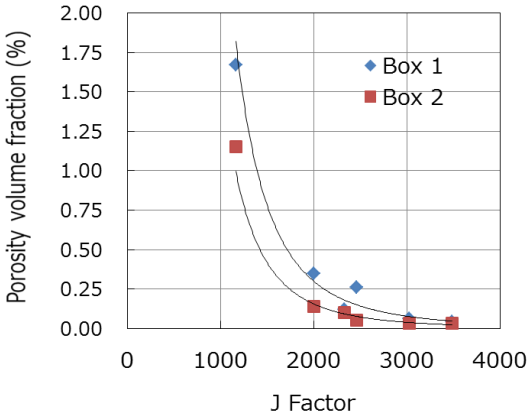

Fig. 3. Relationship between porosity volume fraction and J factor

2.3 Experimental results and research aims

Although a relationship was demonstrated between increased J factor and quantitatively enhanced casting quality, the J factor is an empirical formula that defines the flow of metal as it passes through the gate, whereas the internal quality that we aim to enhance in this experiment is in the thick parts, which are far from the gate. To establish a technique for improving casting

quality by increasing the J factor, the following questions must be clarification.

1. What is the microscopic state of the atomized flow as it passes through the gate?
2. What is the state of the molten metal after injection when it flows into the die as an atomized flow at the gate, and what effect does this state have on reducing the porosity of thicker areas?

Question 1 can be investigated by photographic experiments that capture the metal as it is injected into an open space. For question 2, the internal state of the metal flow cannot be determined by observation because aluminum reflects light. We therefore decided to use the latest CFD techniques to create a simulation to visualize the microscopic flow of the metal. In CFD, a microscopic metal flow is simulated as a two-phase flow of aluminum and air. Because the flow in HPDC is turbulent, turbulence calculations need to be performed in the two-phase flow analysis. We developed a system for performing turbulence calculations of this two-phase flow and investigated the mechanisms underlying the reduction in porosity by increasing the J factor. The following gives an overview of the verification process used in this research.

3 Verification process in this research

3.1. Photography experiment on metal injected into an open space

First, we performed a photographic experiment to clarify the changes in the metal flow interface when it passes through the gate; these changes were defined according to the J factor. The method reported by Aida et al. for injecting metal into an open space was used for the experiment [11]. In HPDC, metal is injected such that its speed is at least 30 m/s while passing through the gate. A pulse laser was used to perform transmission imaging to gain a detailed understanding of the microscopic changes in the metal interface as it moves at high speed. Nanosecond-order exposure was made possible by synchronizing the pulse laser with a high-speed camera. By using transmitted light, the metal flow interface can be clearly imaged without interference from light scattering. We used this imaging technique to perform a comparative investigation of the process by which the droplets were produced at the metal flow interface by atomization while varying the J factor. Furthermore, we measured the size distribution of the generated droplets and used the results to set the resolution (i.e., mesh size) required for simulating this phenomenon.

3.2. Computational investigation of two-phase fluid flow of metal inside die

3.2.1 Development of the simulation system

In the flow analysis currently used in computer-aided engineering of regular casting, the macroscopic filling state of single-phase flows of aluminum is simulated using differential methods and finite volume methods. Because of this, the behavior of air cannot be calculated directly.
In this research, model calculations were performed using high-precision finite volume methods to simulate the two-phase flow of aluminum and air at the microscopic level. Numerical calculations of turbulence were performed by large eddy simulation (LES), and interface changes were numerically simulated by the volume of fluid (VOF) method. In other words, the two-phase flow inside the die was simulated by the LES-VOF method through coupling of the LES and VOF methods.

3.2.2 Governing equations for flow analysis

The numerical model represents the simultaneous unsteady flow of two immiscible, incompressible fluids, each having a constant viscosity and surface tension. Surface tension is taken into account through the continuum surface force (CSF) model, in which the surface force is transformed into a body force which is only non-zero in the interface region of limited thickness. [9,10]

The mass conservation equation is

$$\frac{\partial \rho}{\partial t} + \boldsymbol{\nabla} \cdot (\rho \boldsymbol{U}) = 0. \tag{3}$$

The momentum equation is

$$\frac{\partial \rho \boldsymbol{U}}{\partial t} + \boldsymbol{\nabla} \cdot (\rho \boldsymbol{U}\boldsymbol{U}) = -\boldsymbol{\nabla} P + \boldsymbol{\nabla} \cdot \boldsymbol{\tau} + \boldsymbol{F}_{\mathrm{S}} + \rho \boldsymbol{g}. \tag{4}$$

Here, ρ is density, $\boldsymbol{U}$ is a flow velocity vector, $\boldsymbol{\tau}$ is a viscous stress tension, P is absolute pressure, and $\boldsymbol{g}$ is a gravitational acceleration vector. The $\boldsymbol{F_s}$ term in Eq. (4), follows the CFS model. For the surface tension coefficient σ_s, the phase volume fraction α, the curvature of the two-phase interface k, and a unit normal vector perpendicular to the interface $\boldsymbol{n_s}$, the body force based on the CSF model is given by

$$\boldsymbol{F}_{\mathrm{S}} = \sigma_S + k \boldsymbol{\nabla}_{\alpha}, \tag{5}$$

$$\mathrm{K} = -\boldsymbol{\nabla} \cdot n_s, \quad \boldsymbol{n}_S = \frac{\boldsymbol{\nabla}_{\alpha}}{[\boldsymbol{\nabla}_{\alpha}]} \tag{6}$$

The interface between the phases is simultaneously computed using a surface-capturing methodology that employs the volume fraction of one of the phases (taken here to be liquid-phase) as an indicator function (VOF) to identify the different fluids (surrounding air-phase). The interface is not defined as a sharp boundary, and a transition region exists where the fluid is treated as a mixture of the two fluids on each side of the interface, which in reality is a discontinuous step. When the interface is advected by the flow, the evolution of the VOF advection equation, namely, the transport equation

of the volume fraction of liquid α_l, is given by the following conservative form:

$$\frac{\partial \alpha_l}{\partial t} + \nabla \cdot (\alpha_l \boldsymbol{U}) = 0, \quad (7)$$

where α is the volume fraction, the subscript l represents the aluminum phase, and

$$\alpha_l + \alpha_g = 1, \quad (8)$$

where the air phase is indicated by the subscript g. Using the volume fraction of each phase, density ρ and viscosity coefficient μ are

$$\rho = \alpha_l \rho_l + (1 - \alpha_l)\rho_g, \quad (9)$$
$$\mu = \alpha_l \mu_l + (1 - \alpha_l)\mu_g. \quad (10)$$

3.2.3 System verification method

To investigate the fundamental reproducibility of the atomization phenomena when the new system was being developed, we compared the simulation results with the photography results for the injection state of the metal [9]. Then, we modeled and verified the casting die design used in the casting experiment presented in Section 2. Verification consisted of comparing the relationship of the aluminum filling ratio and J factor of the thicker parts at the pin bosses when filling was complete with the trends between porosity volume fraction and J factor as observed by micro-CT.

4 Photography experiment for metal injection

4.1 Photography method

Figure 4 shows the structure of the die used in the injection experiment and the placement of the light source and camera. Photography was performed by using a pulse laser to illuminate the die from the rear horizontal direction and positioning the camera in front of the die. An acrylic plate was attached to the side of the die to transmit the laser light. The injection experiments were performed using a casting machine with a die cramping force of 350 tons. An Al-11%Si-2.5%Cu-0.2%Mg (JIS ADC12) alloy was used as the injected material to allow comparison with the experiments reported by Aida et al. The laser light was illuminated onto the side of the die from a transmitter via optical fiber. Photography was performed using a high-speed camera at 8000 fps. Figure 5 shows an example plot of injection speed in the experiment with J=3030.

4.2 Photography results

Figure 6 shows the photography results for various J factors. At a J factor of 240, the state of the metal flow interface was a continuous jet and the interface was continuous and smooth. In this flow state, almost no

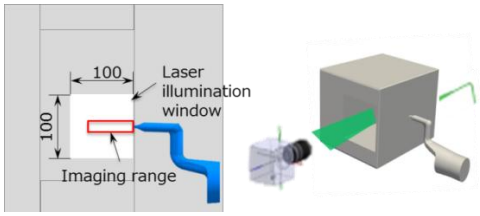

Fig. 4. Layout of the die and photograph equipment for imaging of the injected flow

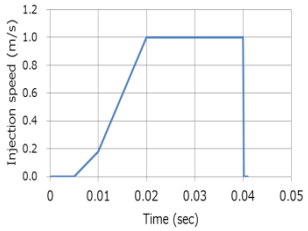

Fig. 5. Injection speed

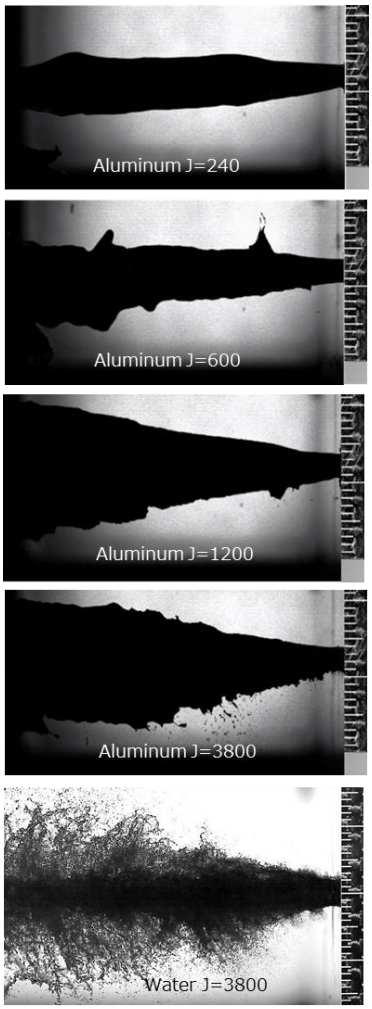

Fig. 6. Pulse laser transmission photography results

vertical spreading of the metal was observed. At a J factor of 600, the metal flow interface began to fluctuate, and the metal flow began to spread in the vertical direction. At a J factor of 1200, which exceeds the threshold for atomized flow, the atomization process was

observed; liquid columns were formed due to K-H instability induced at the metal flow interface and droplets broke off from the liquid columns.
Furthermore, the spread of the metal flow in the vertical direction became larger. At a J factor of 3800, the fluctuations in the metal flow interface further increased and the frequency of droplet generation increased. The photography results for water at a J factor of 3800 are also shown for reference. The internal atomization state could be observed because of the laser light passing through the water. The vertical spreads of water and aluminum were nearly the same. Although the internal state of the aluminum could not be viewed because it is opaque to light, the vertical spread suggests that the atomized flow within the transmission image has a state similar to that of water. Furthermore, whereas the water droplets were spherical, the aluminum droplets were ribbon-shaped.

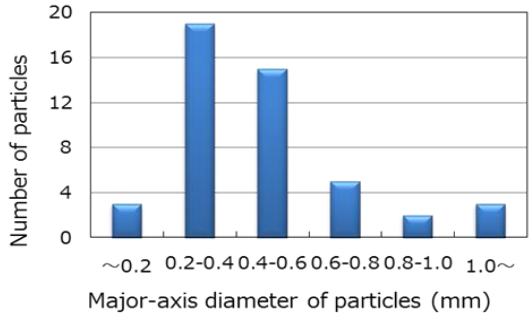

Fig. 7. Major axis diameter distribution of droplets

Figure 7 shows the distribution of the major-axis diameter for the droplets generated from the metal interface. Many droplets of size 0.2 to 0.3 mm were observed. In the atomized flow region defined by the J factor from the above results, a jet flow consisting of a two-phase flow of aluminum and air was formed by atomization upon passing through the gate. Furthermore, the results showed that a fine mesh size with a size of around 0.2 to 0.3 mm was needed for the resolution of the simulation.

5 Simulation system verification

5.1 Computational piston die design model and conditions

Table 1 shows the physical values used in the simulation. LES (Smagorinsky type) was used for the turbulence model. Figure 8 shows the model of the piston part and the boundary conditions. The computational model consisted of the sleeve, runners that branch into two pistons from the sleeve, and two pistons. The sleeve end was taken as the inlet for the moving boundary model.
The measurement results for the plunger speed taken at intervals of 1 ms from the casting experiment were derived for the amount of aluminum fed into the inlet. Furthermore, non-slip boundary conditions with walls were set for the sleeve, runners, and piston component of the inner wall parts. The overflow was not fully modeled but was modeled up to the area where the overflow was modeled from the product up to the minimum cross section of the overflow. This minimum cross-section area was taken as the outlet that opens to the air. The total number of cells in the model mesh was 1 million. The time when the inlet injection speed began to increase from low to high when the metal tip reached the gate was set as 0 s.
The calculations were performed until the plunger speed suddenly decreased after the injection was finished and the flow of the metal inside the die had completely stopped. Note that although the plunger begins to apply pressure after it decelerates in an actual casting machine, the pressurization calculation was not performed in the current simulation in order to clarify the changes in the two-phase flow accompanying the change in metal speed.

Table 1. Physical quantities used in the calculations.

	Aluminum	Air
Kinematic viscosity (m^2/s)	1.77E-06	1.60E-05
Density (kg/m^3)	2550	1.165
Surface tension (kg/s^2)	0.878	–

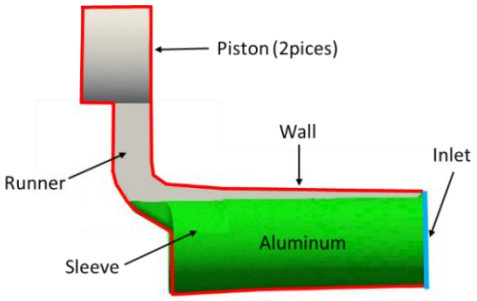

a) Boundary condition

b) Piston calculation model and names of each part

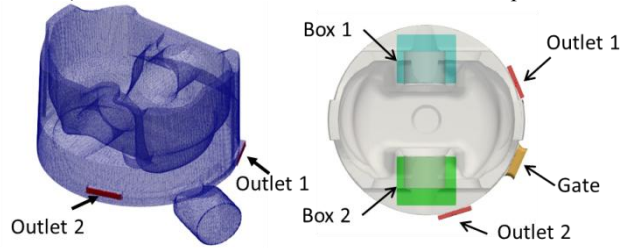

Fig. 8. Casting experiment model, boundary conditions

5.2 Verification of computational results

The validity of the computational model was verified according to whether the relationship between porosity volume fraction and J factor in the cast product was reproduced. Figures 9 and 10 show the filling ratio at each injection time of the parts (Box 1 and Box 2) where the porosity volume fraction was measured by micro-CT.

Figure 11 shows porosity images derived from micro-CT for Box 1 and Box 2. At both Box 1 and Box 2, the rapid increase in the filling ratio and the enhanced filling ratio with increasing J factor were reproduced. Furthermore, the trend of a better filling ratio at Box 2 compared with Box 1 was also reproduced. Note that the difference in maximum filling ratio between Box 1 (90%) and Box 2 (99.5%) was clearly observed in the calculations. These results are discussed in detail in the next section; briefly, the trends in the phenomena investigated here were fully reproduced.

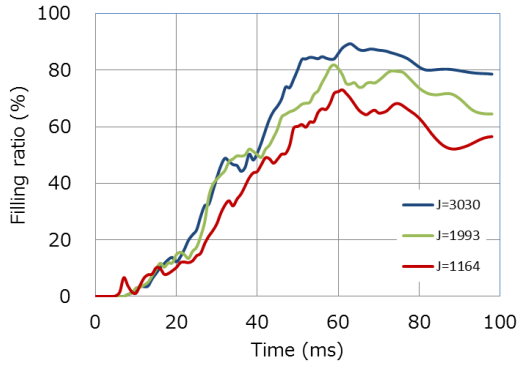

Fig. 9. Changes in the filling ratio at Box 1

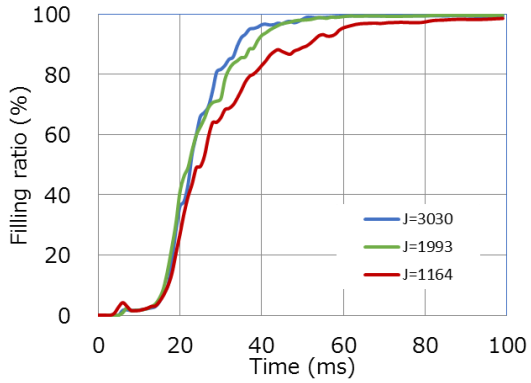

Fig. 10. Changes in the filling ratio at Box 2

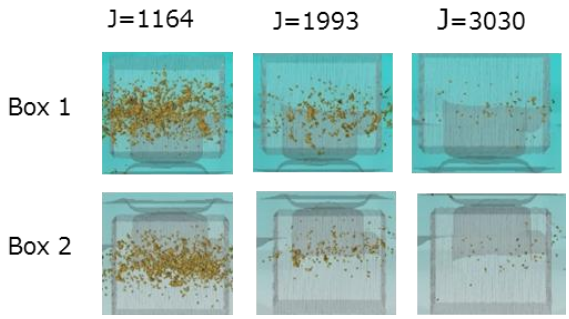

Fig. 11. Porosity images of micro-CT in each Box

6 Discussion of atomized flow by higher J factor

We analyzed the state within the mold when the J factor becomes high enough to produce the atomized flow observed in the experiment involving injection into an open space (see Section 4). The analysis was performed by comparing the computational results for the two injection conditions of J=1164 and J=3030.

6.1 Visualization of flow inside piston by using flow lines

Figure 12 shows the flow lines at 30 ms after acceleration to high speed. The high-speed flow of metal from the gate collides with the piston wall, splits to the left and right, and forms a fast flow from the upper part of the walls of the piston boss part to the outlet (section A). However, the flow speed decreases and the flow toward the outlet weakens in the thick part (section B). Even though the metal is injected at high speed with a high gate speed, there are areas where the flow speed is low. At J=1164 in particular, the speed in the thick part at the pin boss decreases to less than 10 m/s and the flow is observed to stagnate.

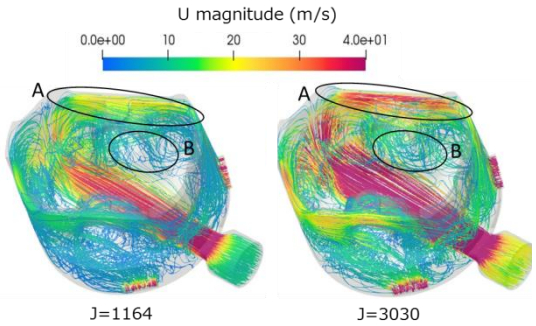

Fig. 12. Flow lines inside the piston (30 ms after acceleration to high speed)

6.2 Changes in the aluminum volume fraction isosurface during the filling process

Figure 13 shows the change in the isosurface of the volume fraction of aluminum α_{AL} = 0.5 from 15 ms after accretion to 30 ms after filling.

In the figure, the scalar value of the velocity is color mapped onto the isosurface. The displayed region shows an area in which there is a substantial amount of entrained air with α_{AL} = 0.5 or less. The changes in the α_{AL} = 0.5 isosurface visualize the void formation process.

Figure 13(a) shows the isosurface at 15 ms after acceleration while the injection is still accelerating. Here, the metal from the gate spreads in the horizontal direction through the entire piston and flows toward the outlet in a mixed state of aluminum and air.

Figure 13(b) shows the isosurface at 30 ms after acceleration when the rate of high-speed injection is constant. In areas where the flow speed from the gate is high, the flow contains little air. Air voids have formed in Box 1 and Box 2 in the thick parts of the piston. These voids are expelled by the gas phase extrusion effect

caused by the negative pressure gradient of the liquid phase in the outlet direction.

Figure 13(c) shows the isosurface at 50 ms after acceleration when the high-speed injection has finished. Because the void on the Box 2 side is near Outlet 2, the air from the void is expelled and the occupancy of voids in Box 2 decreases. In Box 1, the flow of air from the void to Outlet 1 remains.

Figure 13(d) shows the isosurface at 30 ms after the high-speed injection has finished. The filling is complete, the speed of the metal is zero, and the voids inside the product are spherical. These spherical voids form a spherical pore shape called blowholes in HPDC. In actual casting, point D corresponds to pressurization by the casting machine at 30 ms after the injection is finished, and the voids are compressed at a casting pressure of around 60 MPa.

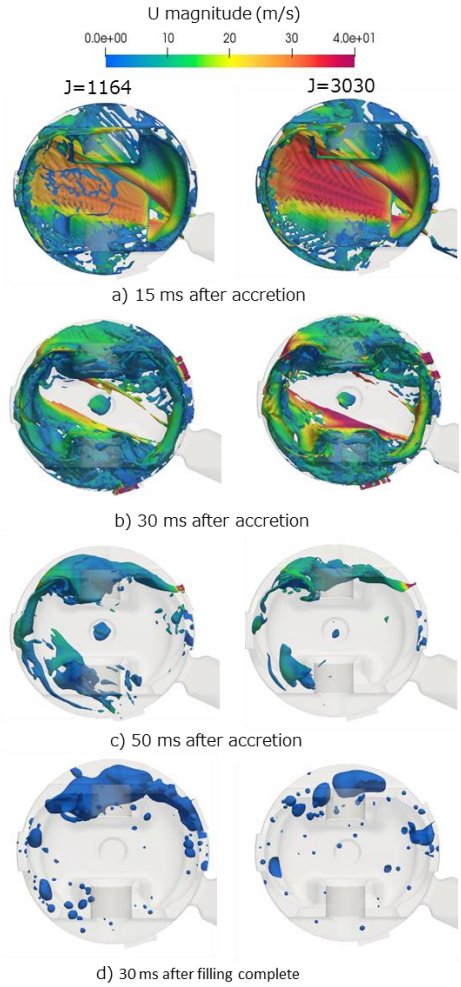

Fig. 13. Void visualization by $\alpha_{AL} = 0.5$ isosurface

6.3 Changes in vortex structure

The HPDC flow is turbulent, and the vortex structure of the turbulent flow is thought to affect the transport efficiency of the air in the two-phase flow of aluminum and air. The vortex structure is difficult to determine through photography experiments but can be identified through numerical calculations. We therefore attempted to visualize the changes in the vortex structure of the metal within the die.

A method that uses the second invariant Q of the velocity gradient tensor has been proposed as a method for identifying vortex structure [12]. The definition of Q is given by Eq. (11).

$$Q \equiv -\frac{1}{2}\frac{\partial u_i}{\partial x_j}\frac{\partial u_j}{\partial x_i} = \frac{1}{2}\left(\|\boldsymbol{\Omega}\|^2 - \|\boldsymbol{S}\|^2\right) \quad (11)$$

Here, $\boldsymbol{\Omega}$ is the vorticity vector and $\boldsymbol{S}$ is the shear velocity vector. The vortex structure can be identified by extracting the isosurface of the region where Q exhibits a positive threshold value. This means that the regions where the rotational motion is larger than the shear motion are extracted as vortex cores. The developed system has the resolution required for calculating a small turbulence vortex using the LES model, which reproduces the atomization phenomena. Because of this, the vortex structure could be visualized using the Q isosurface

Figure 14 shows the changes in the isosurface from 15 ms to 30 ms after accretion. The scalar value of vortex strength, called enstrophy, is color mapped onto the Q isosurface.

At 15 ms after acceleration during injection acceleration (Figure 14a), many small vortices with low vorticity are formed at the position of void formation.

At 30 ms after acceleration when the injection speed is constant (Figure 14b), the small vortices change into longitudinal vortices toward the outlet under the J=3030 condition.

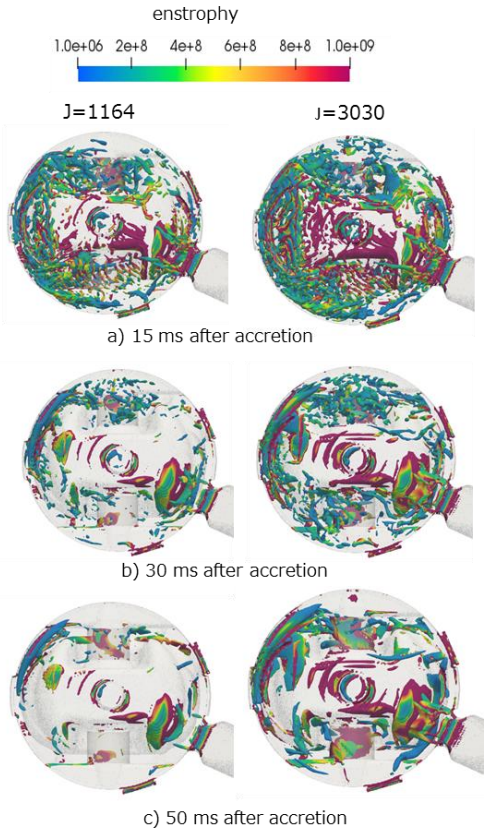

Fig. 14. Visualization of the vortex structure by Q isosurface

On the other hand, the small vortex structure is maintained at the position of void formation under the J=1164 condition.
The formation of a turbulence vortex was observed in the entire metal flow until 50 ms after acceleration when the high-speed injection finished (Figure 14c). For J=1164, the filling is completed with the small vortices remaining in the part of Box 1 with void formation.

The results of the above visualization of the vortex structure clarified the following two points regarding the effect of the J factor on the filling flow characteristics.
1. Under the atomized flow condition, small vortices are generated by turbulent vortices during filling acceleration. Microbubbles are captured near the center of the turbulent vortex due to the pressure gradient in the vortex. The small vortices are maintained in the thick part until filling is complete, and a strong correlation was observed with the presence of porosity.
2. As the J factor is increased, the vortices change from small vortices to those having a structure with a pressure gradient to the outlet. It is thought that the porosity of the thick part is reduced through an effect whereby the microbubbles are expelled to the outlet.

6.4 Quantifying the expulsion of air from the outlet

We next investigate the effect of the changes in vortex structure described in Section 6.3 on the amount of air expelled from the outlet.
The amount of aluminum expelled V_{AL} and the amount of air expelled V_{AIR} were found from Eq. (12) below using the cross-sectional area of the outlet A_{OUTLET}, the speed of the aluminum U_{MAG} at each time, and the aluminum volume fraction α_{AL}.

$$U_{mag} = \sqrt{Ux^2 + Uy^2 + Uz^2}$$

$$V_{AL} = A_{OUTLET} \times U_{mag} \times \alpha_{AL}$$

$$V_{AIR} = A_{Outlet} \times U_{mag} \times (1 - \alpha_{AL}) \qquad (12)$$

Figure 15 shows the amount of air expelled from the outlet at each time (timestep = 1 ms). The expulsion of air reaches a maximum at point A, 15 ms after acceleration. This corresponds to when small air vortices form to the greatest extent as described in Section 6.3. When aluminum flows into Outlet 1 at this time and blocks the expulsion of air, the amount of air expelled from Outlet 2 suddenly increases. After this, the air is expelled from the outlet in a multiphase flow with aluminum. The amount of air expelled at point B when the maximum speed is reached corresponds closely to the changes in vortex structure.
Figure 16 shows the changes in the proportion of air expelled from each outlet. The ratio of the amount expelled from each outlet as the J factor changes is expressed with the maximum amount expelled from Outlet 1 at J=3030 normalized to 100. At point A when the aluminum reaches Outlet 1, 30% to 40% of the air is expelled. After this, at the high J factor of J=3030 at point B when the speed is constant, a multiphase flow with 80% to 90% air is expelled. For effective expulsion of air, it appears important to lengthen the acceleration time and to actively utilize the vortex structure from the turbulence.

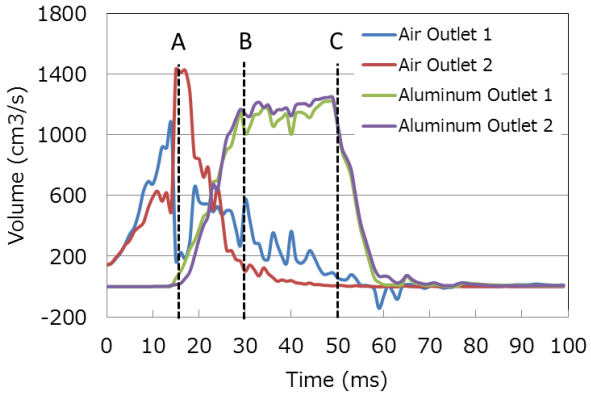

a) J=1164

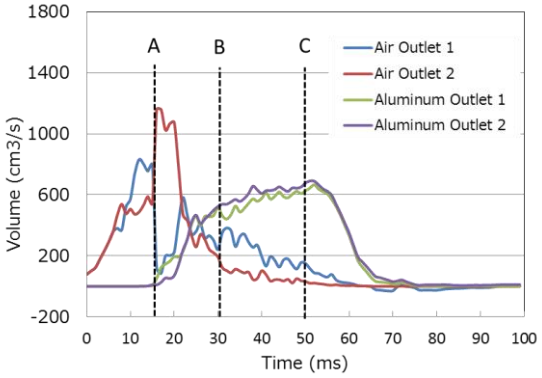

b) J=3030

Fig. 15. Amount of air and aluminum expelled from the outlet.

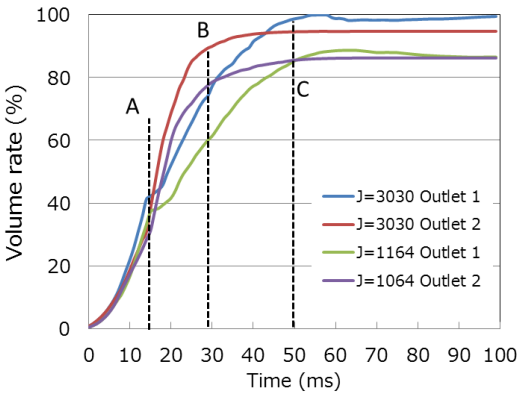

Fig. 16. Proportion of air expelled from the outlet

6.5 Changing the filling pressure

Figure 17 shows the time course of metal pressure in Box 1 and Figure 18 shows the relationship between the maximum metal pressure and J factor.
As the metal flow speed is increased and the J factor is increased, the metal pressure inside the product part increases because the metal flow is constricted at the

outlet. As shown in Figure 18, the maximum metal pressure increases linearly with J factor. Although the actual casting pressure is pressurized up to 70 MPa, around 50 ms is required to reach this pressure. Thus, increasing the metal pressure increases the pressurization effect during the initial pressurization stage.

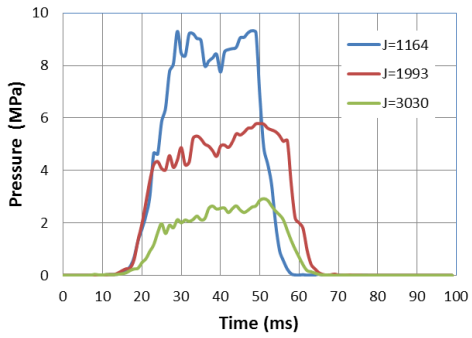

Fig. 17. Time course of metal pressure for various J factors

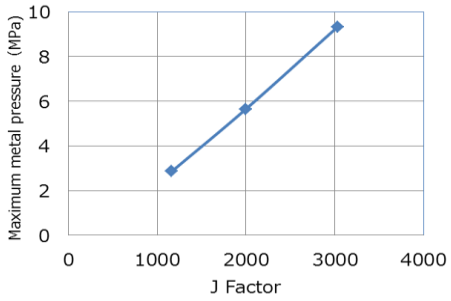

Fig. 18. Maximum metal pressure and J factors

6.6 Sources of porosity

We now discuss the results showing that the differences in filling ratio between Box 1 and Box 2 in the calculations were larger than the differences in porosity volume fraction in the cast products, as described in Section 5.2.

Oxygen was not detected by gas analysis of the cast test pieces, but around 60% nitrogen and 40% hydrogen were detected. Oxygen, which constitutes around 20% of air, undergoes an oxidation reaction with the molten aluminum metal during the filling process and does not remain as a gas in the product. The calculations in the developed system are based on a fixed volume of gas without any changes in composition. Because the air and aluminum form a multiphase flow in the initial filling stage, the decrease in the volume of oxygen gas is thought to decrease at an earlier stage with increasing J factor.

Considering that the volume in Box 1 when the void forms decreases to 20%, the large voids disappear at the maximum filling ratio of 90% for J=3030 and 80% for J=1993, which matches the experimental results.

Figure 19 shows SEM micrographs of the porosity of a piston fabricated in the casting experiment. An SEM micrograph of a 0.25 mm blowhole from air incorporated in regular HPDC is shown for comparison.

The porosity in the test piece was characterized by a small pore size of around 0.1 mm, and clear dendrites were observed. For HPDC, a model has been proposed for the formation of porosity by hydrogen in solid solution emitted between the dendrites during solidification [13].

In HPDC, hydrogen is produced during the filling process by reactions such as those between the mold release agent and the molten metal. Although the filling ratio in Box 2 was 99.5% in the high J factor state and no large voids were observed, fine porosity originating from hydrogen was actually observed. This is attributed to hydrogen or nitrogen being finely dispersed into sizes smaller than the mesh size of the calculation and forming nuclei for porosity. Then, fine porosity is formed when the hydrogen is emitted during the solidification process.

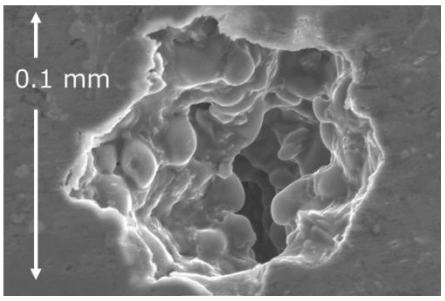

a) Porosity in Box 1 for J = 3030

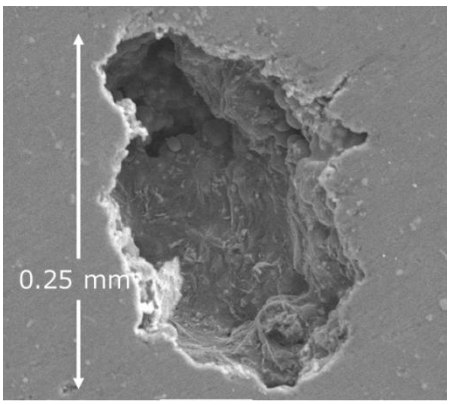

b) Blowhole in regular HPDC

Fig. 19. SEM micrographs of high J factor porosity and a blowhole

7 Conclusion

Experimental results were obtained in which a metal flow passing through the gate formed an atomized flow and the porosity in a HPDC piston was reduced by increasing the J factor. The underlying mechanisms were clarified by analysis of the two-phase flow of aluminum and air using the LES-VOF method for turbulence calculations.

1. In the die cavity, an atomized flow generates small vortices via turbulent vortices during filling acceleration, and these were accompanied by small bubbles near the vortex centers. A strong correlation was observed between the locations of these vortices

and the generation of high porosity in the thick parts.

2. It is thought that the porosity of thick parts can be decreased by changing the vortex structure to longitudinal vortices toward the overflow and decreasing voids by increasing the J factor.
3. We showed the feasibility and utility of visualizing states that cannot be understood from experiments by performing turbulence calculations and accurately solving the state of the multiphase flow in HPDC. This system can be applied to various types of HPDC depending on the definitions of the physical properties of materials.

Acknowledgements: We thank Mr. Youhei Sekiguchi, Mr. Yuki Fujisawa, Mr. Yuji Okada, and Mr. Tomohiro Fujimoto of Honda Foundry Co., Ltd. for performing the casting experiments and collecting the casting data. We also thank Mr. Masanori Tsukamoto of Softflow Co., Ltd. for support with post-processing of the calculation results by POSTFLOW.

References

1. A. Tanihata, N. Sato, K. Katsumata., T. Shiraishi, SAE 2006-01-098 (2006)
2. M.Suzuki, SETC 2006-32-0031
3. T. Kaneuchi, H. Nakano, J-DE JD08-20 (2008)
4. Y. Yamada, H. Yoshi, S. Mochizuki, et al.,SETC 2011-32-0504 (2011)
5. S. Aida, I. Kuboki, Y. Hayashi, M. Fujimoto, et al., J-DE Transactions, JD12-8 (2012).
6. I. Takahashi, K. Anzai, M. Itamura, Reports of 170th J.JFS Meeting, p 21 (2017).
7. E.Koya, M. Nakagawa, S. Kitagawa, J. Ishimoto ,Y. Nakano, N Ochiai, SAE, 2018-01-1393, (2018)
8. E.A.Herman, NADCA, "GATING MANUAL" , p35-36, Publication #5
9. J. Ishimoto, T. Sato, A. Combescure, IJHE, Vol42, Issue 15 (2017)
10. J. Ishimoto, F. Sato, G. Sato, JEGTP Vol.132, 082801 (2010)
11. E.Koya, M. Nakagawa, S. Kitagawa, J. Ishimoto ,Y. Nakano, N Ochiai, SAE, 2018-01-1392, (2018)
12. J.C.R.Hunt, A.A. Wray, P.Morin, Center for Turbulence Research CTR-88, p193, (1988)
13. K.Kubo, J-JFES, 78, p620 (2006)